



# Framework Ti-rich titanium silicalite-1 zeolite nanoplates for enhanced photocatalytic H<sub>2</sub> production from CH<sub>3</sub>OH

Pengxian Tao<sup>a</sup>, Xiao Wang<sup>a,\*</sup>, Qiao Zhao<sup>b</sup>, Hongxia Guo<sup>a</sup>, Li Liu<sup>a</sup>, Xiwei Qi<sup>a,\*</sup>, Wenquan Cui<sup>a,\*</sup>

<sup>a</sup> Hebei Provincial Key Laboratory of Environmental Photocatalytic and Electrocatalytic Materials, College of Chemical Engineering, North China University of Science and Technology, Tangshan 063210, PR China

<sup>b</sup> School of Materials Science and Engineering, National Institute for Advanced Materials, TKL of Metal and Molecule-Based Material Chemistry, Nankai University, Tianjin 300350, PR China

## ARTICLE INFO

### Keywords:

Titanium silicalite-1

Ti-rich

Photocatalytic H<sub>2</sub> production

Structure-activity relationship

Actual active sites

## ABSTRACT

As a successful industrial catalyst, titanium silicalite-1 zeolite (TS-1) also possesses unique photocatalytic activity, but still challenging due to the unsatisfactory activity and unclear photocatalytic mechanism. Here, we achieved the optimization of TS-1 in both the morphology and content of framework Ti by a facile dual-structure directing agent method. The Ti-rich TS-1 nanoplates exhibit enhanced photocatalytic H<sub>2</sub> production performance from methanol. The structure-activity relationship was revealed that the nanoplate-like morphology is beneficial to the photocatalytic activity, owing to the largely retainment of photogenerated electrons. Combined with in-situ DRIFTS and theoretical calculations, it is proposed that Ti–O group would function as a whole to serve as the active site, rather than separated Ti and O sites for reduction and oxidation half reactions respectively. The formation of hydroxylated Ti can also promote the photocatalytic performance. These insights into the mechanisms suggest the great potential of Ti-rich TS-1 nanoplates as commercial photocatalytic materials.

## 1. Introduction

Photocatalysis has been considered as a promising solution to current energy and environmental issues for decades [1]. Numerous efforts have been devoted to the design of efficient photocatalysts, based on metal oxide/sulfide semiconductors [2], MOFs [3], C<sub>3</sub>N<sub>4</sub> [4], etc., as well as the development and fabrication of other novel photocatalysis materials. In addition, researchers are devoting efforts to probe and understand the underlying photocatalytic mechanisms at the micro-level, by which can guide the modification and improvement of existing photocatalysts [5]. For example, it is found that some special microstructures generated by interfacial engineering or intermediate valence states exhibit high performance [6,7]. Besides, researchers are also working to address the low energy conversion efficiency and low visible light utilization, with strategies including construction of heterojunction [8] and energy band engineering [9]. However, despite decades of excellent work in the field, much still needs to be done to meet the demand for industrialization of photocatalysis technology. So far, the large-scale production and application of photocatalysts is challenged by harsh synthesis conditions, unstable structures, photocorrosion, difficulties in recycling powder catalysts [10,11], etc. So far,

only a few materials, such as P25, have been commercialized. Therefore, it is critical to develop basic photocatalytic materials (or supports and platforms for other photocatalysts) with high activity, stability, reusability and recyclability, which can be rapidly commercialized.

Zeolites are the most widely used materials in industrial catalysis, but their great potential for photocatalysis has not received enough attention. Isolated metal oxide (Ti, V, Cr, and Mo-oxides) moieties with tetrahedral coordination geometry embedded in heteroatom-containing zeolites can be regarded as "single-site heterogeneous catalyst (SSHC)" [12]. As shown in Eq. (1), the photocatalytic activities of SSHC are attributed to ligand-to-metal charge transfer (LMCT) process from oxygen (O<sup>2-</sup>) to Mn<sup>n+</sup> ions, resulting in the formation of charge-transfer excited state (M<sup>(n-1)+</sup>–O<sup>-</sup>) [13]. Such excited electron hole pairs localized within a quite short distance exhibit unparalleled photocatalytic property. For example, the photocatalytic activity of tetrahedrally coordinated Ti in titanium silicalite-1 (TS-1) zeolite, which is the most representative one of SSHC, is much higher than that of octahedrally coordinated Ti in TiO<sub>2</sub> semiconductor [14]. It is also reported that the photocatalytic performance of TiO<sub>2</sub> or P25 can be improved by increasing the content of tetrahedrally coordinated Ti existed in the interfaces [15,16]. Another advantage of TS-1 as an SSHC is the high

\* Corresponding authors.

E-mail addresses: [wangxiao@ncst.edu.cn](mailto:wangxiao@ncst.edu.cn) (X. Wang), [qxw@neuq.edu.cn](mailto:qxw@neuq.edu.cn) (X. Qi), [wqcui@ncst.edu.cn](mailto:wqcui@ncst.edu.cn) (W. Cui).

<https://doi.org/10.1016/j.apcatb.2023.122392>

Received 19 November 2022; Received in revised form 17 December 2022; Accepted 8 January 2023

Available online 9 January 2023

0926-3373/© 2023 Elsevier B.V. All rights reserved.

product selectivity due to homogeneous active sites [17]. In addition, TS-1 possesses superior advantages over conventional semiconductor photocatalysts in aspect of thermal stability, recyclability, abundant pore structures, large specific surface [18,19], and hence shows the potential in promoting the industrialization and commercialization of photocatalytic technology.



However, TS-1 based photocatalysts are relatively less developed, and the largest limitation is the lack of active sites, namely the framework Ti. Due to the difficulty of synthesis, the content of framework Ti is generally low (< 3 wt%) [20], resulting in the low activity per unit mass. In addition, the mechanism of TS-1 in photocatalysis is not well understood. Much of the relevant research effort has been focused on the reduction reactions that occurred at Ti sites, including H<sub>2</sub> evolution [21] and CO<sub>2</sub> reduction [22,23], but the oxidation half-reactions have rarely been investigated. In some of the previous works, the coordinated O atoms adjacent to Ti are assumed to be the active sites for oxidation reactions [24]. However, it is known that these O atoms in the framework of TS-1 are saturated coordinated and chemically inert, and are difficult to act as adsorption and activation sites for reactants. Hence, the actual processes and sites for oxidation half-reactions in TS-1 are still unclear. Considering that some sacrificial reagents (especially CH<sub>3</sub>OH) are also hydrogen carriers and raw chemical materials [25,26], it is meaningful to investigate the whole reaction process and reaction mechanism on TS-1. Besides, it is well known that the performance of TS-1 is strongly influenced by the particle morphology and microstructure. For example, TS-1 with a small size, morphology of aggregates, or hierarchical pore structure would be highly favorable for thermal catalysis [27,28], but the relationship between morphology and photocatalytic activity in TS-1 has not been investigated to the best of our knowledge. Therefore, it is crucial to address these key scientific questions in order to extend the application of TS-1 in photocatalysis.

In this work, in order to improve the photocatalytic performance of TS-1, we developed a dual-structure directing agent (dual-SDA) method, and investigated the regulation mechanism by a series of characterizations. The extra addition of cetyltrimethylammonium bromide (CTAB) as the secondary SDA plays a significant role in regulating both the morphology and framework Ti content of TS-1. In aqueous methanol solution, the optimal Ti-rich TS-1 nanoplates catalysts (1 C-TS-1) exhibit enhanced photocatalytic H<sub>2</sub> production performance (more than 30-fold than unmodified TS-1), in particular the activity exceeds that of anatase TiO<sub>2</sub>, and is comparable to the commercial P25. The structure-activity relationship of TS-1 in photocatalysis was investigated for the first time by a series of photoelectrochemical characterizations. The reaction mechanism and the actual photocatalytic active sites in TS-1 were also investigated by in-situ DRIFTS and theoretical calculations. The results provide a new insight into the theory of TS-1 as a photocatalyst, and suggest the great potential of Ti-rich TS-1 nanoplates as commercially

available photocatalytic materials.

## 2. Experimental section

### 2.1. Catalyst preparation

As illustrated in Scheme 1, TS-1 samples were synthesized by hydrothermal method [29] with the extra addition of CTAB. Tetrabutyl orthotitanate (TBOT, 0.175 mL) was firstly dissolved in isopropyl alcohol (IPA, 5 mL), and then mixed with tetrapropylammonium hydroxide solution (TPAOH, 2.0 M, 2 mL) and stirred for 0.5 h. In another procedure, TPAOH (2.0 M, 4.4 mL) and different amount of CTAB were added gradually to the tetraethyl orthosilicate (TEOS, 5 mL) with vigorously stirring for 0.5 h. Subsequently, the above two solutions were mixed and stirred for 5 h, and then heated at 353 K for 30 min to sufficiently remove the ethanol existing in the system and compensated with water. Then the as-obtained mixture was transferred into a PTFE lined autoclave and crystallized at 443 K for 48 h. The sample was cooled to room temperature and the precipitate was separated and washed with water until pH = 7.5. The recovered solid was dried at 373 K for 12 h and then calcined at 823 K for 6 h. The obtained samples are denoted as xC-TS-1, where x refers to the molar ratio of 700 × CTAB/TEOS, x = 0, 0.5, 1, 2, 5, 10, 20 and 30.

### 2.2. Catalyst characterization

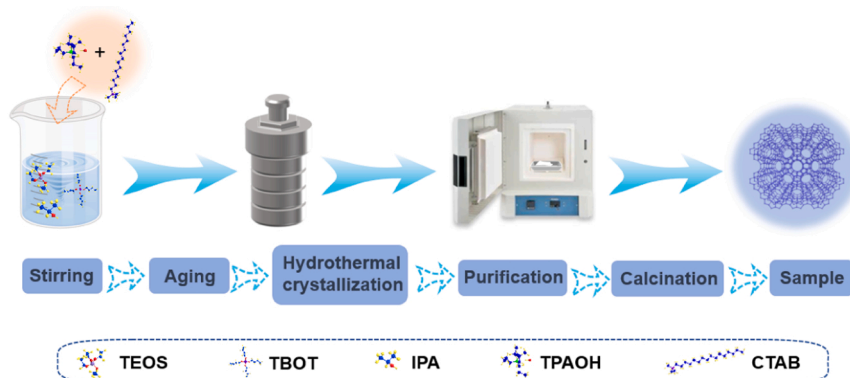
The X-ray diffraction (XRD) patterns were recorded on a Bruker D/max-2500PC diffractometer with a Cu Kα radiation (λ = 1.5406 Å). The relative crystallinities were calculated by comparing the summed intensities of the XRD peaks.

Scanning electron microscopy (SEM) images were taken on a Hitachi S-4800 electron microscope.

Transmission electron microscopy (TEM) images were obtained on a JEM-2800 F electron microscope at an accelerating voltage of 200 kV. EDX-mapping images in the dark field were acquired to analyze the element distribution.

N<sub>2</sub> adsorption/desorption isotherms were measured on a Micromeritics ASAP 2460 analyzer at 77 K after degassed at 573 K for 10 h. The total specific surface area (S<sub>BET</sub>) was derived from the Brunauer-Emmett-Teller (BET) equation. The external surface area (S<sub>ext</sub>) was derived from the *t*-plot method, and the micropore surface area (S<sub>micro</sub>) was calculated by subtracting S<sub>ext</sub> from S<sub>BET</sub>. The total pore volume (V<sub>total</sub>) was obtained from the absorption amounts calculated at *p/p*<sub>0</sub> = 0.99. The micropore volume (V<sub>micro</sub>) was also derived from the *t*-plot method, and the mesopore volume (V<sub>meso</sub>) was calculated by subtracting V<sub>micro</sub> from V<sub>total</sub>. The pore size distribution was determined by NLDFT method.

The elemental compositions were measured by an inductively coupled plasma optical emission spectrometer (ICP-OES, Perkin-Elmer



Scheme 1. Schematic illustration of the synthesis of xC-TS-1 catalysts.

Optima 5300DV).

Ultraviolet-visible diffuse reflectance spectra (UV-vis DRS) were recorded on a Persee TU-1901 UV-vis spectrometer with BaSO<sub>4</sub> as a reference.

Fourier transform infrared (FTIR) spectra were recorded on a Bruker Vertex70 spectrometer.

Raman spectra were collected using a Renishaw Invia Raman spectrometer (514 nm excitation).

X-ray photoelectron spectra (XPS) were measured by a Thermo ESCALAB 250 Xi instrument with an Al K $\alpha$  (1486.6 eV) monochromatic X-ray source.

Fluorescence spectra were measured by a Hitachi F-7000 fluorescence spectrophotometer with excitation at 270 nm. Transient state fluorescence spectra were measured on an Edinburgh Instruments FS5 spectrometer. Double exponential fitting was performed and the fluorescence lifetime was estimated by the weighted average of the fitting, and the value of the average lifetime was evaluated based on the following equation:

$$\tau_{avg} = \frac{\tau_1 B_1^2 + \tau_2 B_2^2}{\tau_1 B_1 + \tau_2 B_2} \quad (2)$$

Photoelectrochemical (PEC) measurements were conducted on a Chenhua CHI660E electrochemical workstation with a three-electrode system.

*In-situ* diffuse reflection infrared Fourier-transform spectroscopy (DRIFTS) measurements were carried out on a Bruker TENSOR II spectrometer equipped with a MCT detector. The samples were first dried at 373 K and the background spectrum was collected. Then the sample chamber was vacuumized and filled with methanol vapor and water vapor in a ratio of 1:1 under dark conditions and the infrared spectra were recorded. Subsequently, the light started and the infrared data spectra were recorded continuously.

### 2.3. Catalytic performance test

The photocatalytic H<sub>2</sub> production experiments were carried out under UV irradiation. Before each test, 20 mg catalyst was dispersed in 30 mL of aqueous methanol solution at different concentrations. The reactions were conducted using a photocatalytic H<sub>2</sub> production system (CEL-PAEM-D8plus, Beijing China Education Au-Light Co., Ltd.). The reaction solution was evacuated for 20 min to completely remove the air prior to irradiation under a 500 W mercury lamp. The temperature of the reaction solution was maintained at 298 K using a flow of cooling water during the reaction. The amount of H<sub>2</sub> produced was analyzed by an on-line gas chromatograph equipped with a TCD detector (GC7920). The amount of liquid products was analyzed by a gas chromatograph equipped with a FID detector, and the amount of formic acid was analyzed by an ion chromatograph (OIC-600).

The turnover frequency (TOF, per mole Ti) and the rate of H<sub>2</sub> production (i.e., mass activity) of different Ti-based catalysts were calculated according to Eqs. (3) and (4), respectively. The efficiency of the photocatalytic reaction was also evaluated in terms of an apparent quantum yield (AQY), defined by Eq. (5).

$$TOF(h^{-1}) = \frac{\text{Moles of H}_2 \text{ produced (mmol)}}{\text{Moles of Ti atoms (mmol)} \times \text{Time (h)}} \quad (3)$$

$$\text{H}_2 \text{ production rate (mmol} \cdot \text{g}^{-1} \cdot \text{h}^{-1}) = \frac{\text{Moles of H}_2 \text{ produced (mmol)}}{\text{Moles of catalysts (g)} \times \text{Time (h)}} \quad (4)$$

$$AQY(\%) = \frac{\text{Number of evolved H}_2 \text{ molecules} \times 2}{\text{Number of incident photons}} \times 100\% \quad (5)$$

### 2.4. Computational methods

All the calculations within a periodic cell are performed in the

framework of the density functional theory by Dmol<sup>3</sup> package [30,31]. The generalized gradient approximation proposed by Perdew, Burke, and Ernzerhof is selected for the exchange-correlation potential. The long range van der Waals interaction is considered by a DFT-D correction. The inner electrons of Ti are treated DFT Semi-core Pseudopotentials [32], and the electrons of other atoms are in all-electron calculation. The Brillouin zone integration is performed using a  $1 \times 1 \times 2$  Monkhorst-Pack grid. For geometry optimization, convergence tolerance is  $1 \times 10^{-4}$  hartree in energy,  $2 \times 10^{-2}$  hartree Å<sup>-1</sup> in force, and  $5 \times 10^{-2}$  Å in displacement. A 96 T cluster model (Si<sub>95</sub>TiO<sub>192</sub>) was selected as a standard structure of zeolite which was extracted from the crystal structure data, and Ti atom was substituted on T1 location in the 10-membered ring [33]. The dangling bonds of the boundary O atoms in the cluster were saturated by H atoms. In order to minimize cluster boundary effects and better simulate the overall zeolite structure, the coordinates of these terminal OH groups were constrained. The terminal O atoms were constrained at their original positions in the MFI unit cell. The adsorption energy ( $E_{ads}$ ) and reaction energy ( $E_{react}$ ) are defined as following equations:

$$E_{ads} = E_{MFI+ \text{molecule}} - E_{MFI} - E_{\text{molecule}} \quad (6)$$

$$E_{react} = E_{\text{product}} - E_{\text{reactant}} \quad (7)$$

## 3. Results and discussion

### 3.1. Optimization of TS-1 catalysts by dual-structure directing agent method

Different with the traditional synthesis method using TPAOH as template, xC-TS-1 catalysts were synthesized by a dual SDA method with the additional addition of CTAB. A series of characterizations were conducted to investigate the synthesis mechanism, especially the function of CTAB.

#### 3.1.1. Effect of CTAB on morphology and textural properties of xC-TS-1 catalysts

As shown in Fig. 1a, all the xC-TS-1 samples exhibit the characteristic diffraction peaks of MFI structure [34], indicating the formation of TS-1. However, the morphology of xC-TS-1 samples was greatly influenced by the addition of CTAB, as shown by TEM images in Fig. 1b and SEM images in Fig. S1. 0 C-TS-1 exhibits morphology of spherical aggregates, while 0.5 C-TS-1 and 1 C-TS-1 samples synthesized with small amount of CTAB exhibit nanoplate morphology with relatively intact crystal structure. Different with conventional six-prism-like morphology of MFI-type zeolites [35,36], the 1 C-TS-1 nanoplate shows elliptical morphology with smooth surface, and the length along *b*-axis (100 nm) is much shorter than that along *a*-axis (700 nm) and *c*-axis (400 nm). The XRD peak intensities of 1 C-TS-1 also become stronger (Fig. 1a), and the relative crystallinity increase to 141% compared with 0 C-TS-1 which is taken as 100% (Table 1), indicating that CTAB can promote the crystallization of TS-1. Besides, 1 C-TS-1 sample exhibits predominance of *h0l* reflections [37,38] due to the good crystallinity of the planes along *a*- and *c*-axis and the loss of long-range order along *b*-axis compared with other aggregates samples, indicating its nanoplate-like structure. With further increase of CTAB amount, the xC-TS-1 samples ( $x \geq 2$ ) obviously change into aggregates morphology once again, and the XRD peak intensities and relative crystallinities decrease, suggesting that the excess CTAB may exert negative effect on the crystallization process. When the amount of CTAB is too much, the morphology exhibits hybrid of rod-like crystals and irregular aggregates (30 C-TS-1 in Fig. 1b). This may be due to the broken crystallization process (relative crystallinity decreases to 82% for 30 C-TS-1 in Table 1) caused by the competition between CTAB and TPAOH, because similar irregular morphologies are often observed in zeolites synthesized by multi-templates [39,40]. All the above results indicate that addition of CTAB as the second SDA is responsible for the

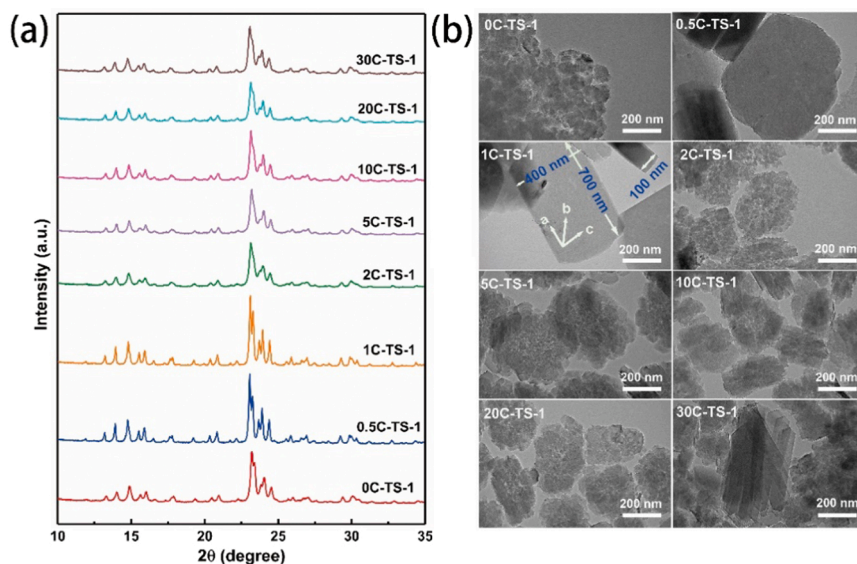


Fig. 1. Textural characterizations of xC-TS-1 catalysts: (a) XRD patterns and (b) TEM images.

Table 1

Textural properties of xC-TS-1 catalysts.

Samples	RC <sup>a</sup>	Surface area (m <sup>2</sup> /g)			Pore volumes (cm <sup>3</sup> /g)		
		S <sub>BET</sub>	S <sub>Micro</sub>	S <sub>Ext</sub>	V <sub>Total</sub>	V <sub>Micro</sub>	V <sub>Meso</sub>
0 C-TS-1	100	502	368	133	0.446	0.205	0.281
0.5 C-TS-1	140	468	406	75	0.241	0.228	0.091
1 C-TS-1	141	482	403	64	0.259	0.209	0.076
2 C-TS-1	103	496	428	68	0.274	0.234	0.096
5 C-TS-1	92	461	393	68	0.271	0.214	0.108
10 C-TS-1	96	478	412	65	0.257	0.217	0.088
20 C-TS-1	88	468	401	67	0.262	0.217	0.095
30 C-TS-1	82	483	361	122	0.374	0.209	0.215

<sup>a</sup> Relative crystallinity.

change in morphologies and crystallinities of xC-TS-1 samples.

In order to reveal the effect of CTAB on the morphology of TS-1, the crystallization processes were stopped at different stages without or with the addition of CTAB. The SEM images and corresponding XRD patterns of the representative samples are shown in Fig. 2. In the crystallization process of 0 C-TS-1 (Fig. 2a and b), no crystals were formed after crystallization for 3 h. After 6 h, the crystal nuclei were formed and gradually grew to aggregates. But in the crystallization process of 1 C-TS-1 (Fig. 2c and d), the crystal nuclei have already formed after 3 h, and then mainly grew along  $\alpha$ -axis and  $c$ -axis to form nanoplate-like crystals. This phenomenon clearly indicates that CTAB can promote the crystal nucleation process and subsequent crystallization process, consistent with aforementioned relative crystallinity results in Table 1.

The N<sub>2</sub> adsorption-desorption isotherms and pore size distribution curves of xC-TS-1 zeolites are shown in Fig. 3, and the textural properties are summarized in Table 1. 0 C-TS-1 sample shows significant adsorption in the low-pressure region ( $p/p_0 < 0.01$ ), consistent with the microporous structure of TS-1. The volume of N<sub>2</sub> adsorbed in the high relative pressure range (0.9–1.0) rises rapidly, and the adsorption-desorption isotherm exhibits hysteresis loop which is hybrid of type I and IV, indicating that the samples also contain mesopores which may be originated from inter-crystal voids in the aggregates. However, a slight decrease in the specific surface area is observed for 0.5 C-TS-1 and 1 C-TS-1 samples, and the mesoporous characteristics nearly completely disappeared which can be demonstrated by the absence of hysteresis loops (Fig. 3a) and micropore size distribution (Fig. 3b), as well as low mesopore volumes (Table 1). This result is unexpected because CTAB is one of the most commonly used pore-expanding agents in zeolite

synthesis [41,42]. It should be noted that with further increase of CTAB amount, especially the 30 C-TS-1 sample, adsorption hysteresis loop appears once again, with both total and extra specific surface area as well as mesopore volumes increased. Therefore, it can be concluded that in our work, small amount of CTAB does not have a pore expanding effect, but can promote the formation of nanoplate-like morphology and the crystal nucleation process and subsequent crystallization process; while larger amount of CTAB can indeed contribute to the pore expanding.

### 3.1.2. Effect of CTAB on framework Ti content

Ti active sites in the framework of TS-1 zeolite are critical to the catalytic performance, both in thermal catalysis and photocatalysis. Hence, a series of methods were used to investigate the influence of CTAB on the distribution and composition states of Ti elements in TS-1. The EDS mapping images in Fig. S2 reveal the homogeneous distributions of Ti element throughout all the xC-TS-1 samples. The total element contents acquired by ICP in Table 2 shows that the mass fraction of Ti in xC-TS-1 samples are 3.2 wt%, 7.2 wt%, 7.8 wt%, 8.2 wt%, 8.2 wt%, 8.3 wt%, 8.6 wt% and 7.5 wt% for  $x = 0, 0.5, 1, 2, 5, 10, 20$  and 30, respectively.

Further characterizations were conducted to distinguish the framework Ti and extra-framework Ti. UV-vis DRS spectra (Fig. 4a) show that each xC-TS-1 sample exhibits a strong absorption band around 215 nm attributed to the charge transfer from O<sup>2-</sup> to Ti<sup>4+</sup> [43], demonstrating the dominantly existence of isolated tetrahedrally coordinated Ti atoms incorporated into the zeolite framework, i.e., framework Ti. Besides, the densities of framework Ti peaks increase with increase of amount of CTAB addition, indicating the increasing amount of framework Ti. The intensities of peaks at 270 nm and 320 nm attributed to amorphous Ti and anatase TiO<sub>2</sub> [44] also gradually increase with increase of CTAB addition, indicating that addition of too much CTAB inevitably brings some extra-framework Ti. As shown in FT-IR spectra (Fig. 4b), all the samples exhibit peaks at 960 cm<sup>-1</sup> caused by the stretching vibration of Si–O–Ti bond, which can be assigned to framework Ti [45], and the densities firstly increased with increase of CTAB addition and then decreased with excess CTAB. The densities of peaks at 530 and 1125 cm<sup>-1</sup> in Raman spectra (Fig. S3) attributed to framework Ti [46] also exhibit similar trend of first increasing and then decreasing with addition of CTAB. XPS was further carried out to determine the surface element compositions and metal oxidation states. As shows in Fig. 4c, in the Ti 2p spectra, the peaks at 460.0 eV and 458.5 eV are assigned to



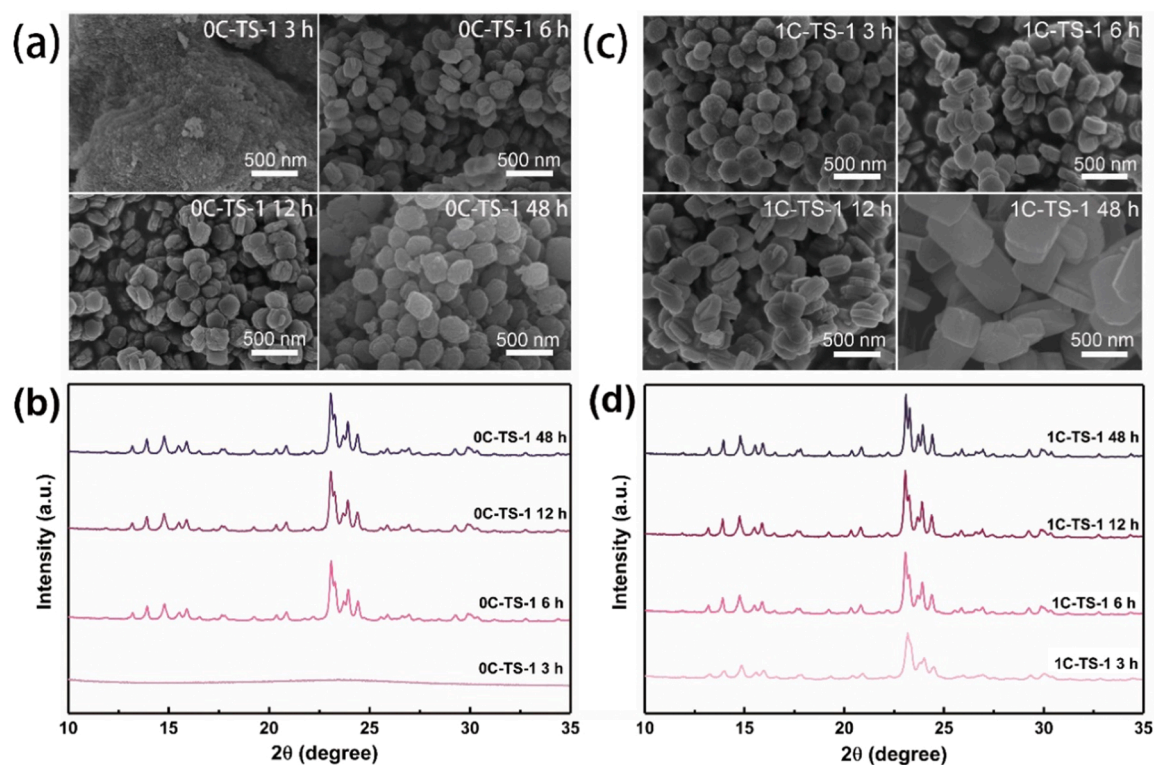


Fig. 2. (a) SEM images and (b) XRD patterns of 0 C-TS-1 samples crystallized for different time; (c) SEM images and (d) XRD patterns of 1 C-TS-1 samples crystallized for different time.

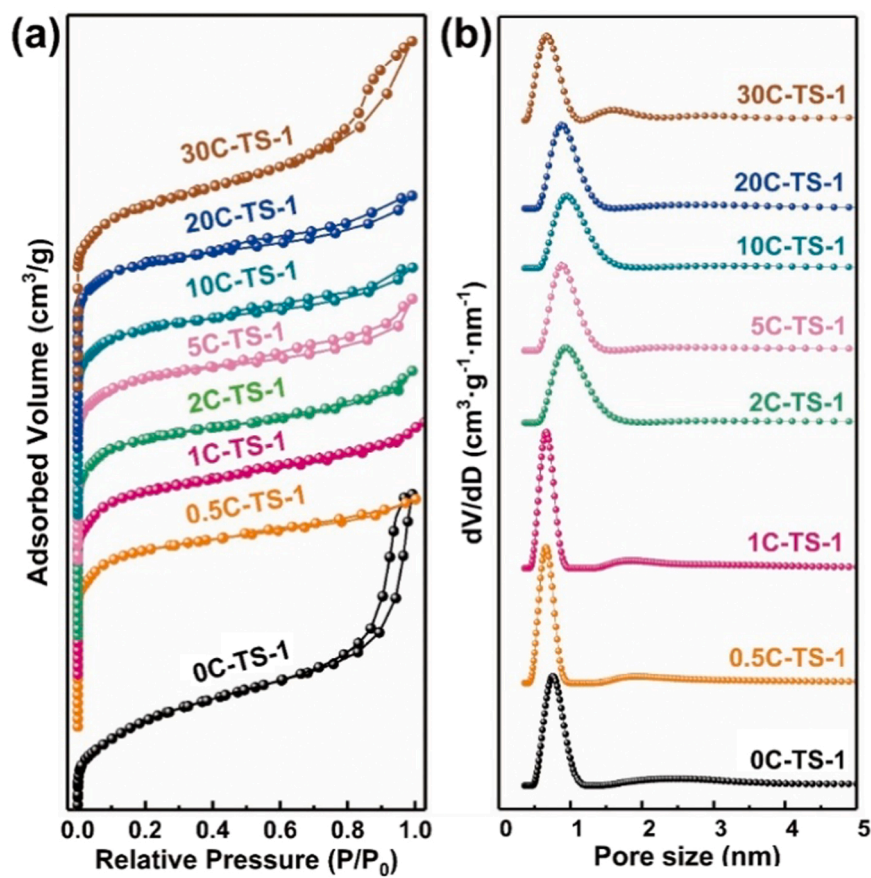


Fig. 3. (a) N<sub>2</sub> adsorption-desorption isotherms and (b) Pore size distribution based on NLDFT of xC-TS-1 samples.

**Table 2**  
Distribution of Ti Species in xC-TS-1 samples.

Catalysts	Content of Ti (wt%) <sup>a</sup>	Ti species contents from XPS (wt%) <sup>b</sup>		Ti species contents from UV-vis (wt%) <sup>c</sup>	
		frame-Ti	extra-Ti	frame-Ti	extra-Ti
0 C-TS-1	3.2	78.2	21.8	68.3	31.7
0.5 C-TS-1	7.2	83.8	15.3	73.4	26.6
1 C-TS-1	7.8	84.7	16.2	71.2	28.8
2 C-TS-1	8.2	92.9	7.1	74.5	25.5
5 C-TS-1	8.2	90.0	10.0	78.2	21.8
10 C-TS-1	8.3	78.0	22.0	52.5	47.5
20 C-TS-1	8.6	43.3	56.7	44.9	55.1
30 C-TS-1	7.5	35.6	64.4	43.5	56.5

<sup>a</sup> Determined by ICP;

<sup>b</sup> Quantified by the ratio of peak areas of framework Ti (460 eV) and extra-framework Ti (458.8 eV);

<sup>c</sup> Quantified by the ratio of peak areas of framework Ti (215 nm) and extra-framework Ti (270 and 330 nm).

framework Ti and extra-framework Ti respectively [47]. It can be observed that the amount of framework Ti significantly increased with addition of CTAB. And for 20 C-TS-1 and 30 C-TS-1, most of the Ti species on the surface are extra-framework Ti, probably due to the low relative crystallinity and coated surface by amorphous Ti. The contents of different Ti species were analyzed quantitatively or semi-quantitatively via aforementioned characterizations, and the results are shown in Table 2 and Fig. 4d. All the results demonstrate the function of CTAB in promoting the incorporation of Ti in the framework of TS-1, as well as the homogenous distribution of Ti atoms in both bulk and surface of TS-1.

### 3.1.3. Mechanism of dual-SDA method in regulating the morphology and framework Ti content of TS-1

CTAB is commonly used to promote pore expansion and formation of hierarchical pore structures in microporous zeolites [48]. However, CTAB may also produce other effects, and the mechanism is ambiguous. In this work, CTAB plays a significant role in regulating both the morphology and framework Ti content of xC-TS-1, and the schematic illustration of the synthesis mechanism is presented in Fig. 5. In terms of morphology, as discussed in Section 3.1.1, small amount of CTAB has no pore expanding effect, but can promote the formation of nanoplate-like morphology. CTAB is a surfactant with a hydrophobic alkyl chains tail and a hydrophilic ammonium ions head. Similar with the multi-quaternary ammonium (e.g., TPAOH), the hydrophilic ammonium ions in CTAB might also interact with Si precursor and act as a secondary SDA [49]. It has been reported that CTAB can stably adsorbed on specific plane surfaces, and the long-chain alkyl group (2.17 nm) occupies the straight channels along the *b*-axis, supported by DFT calculations [48]. Hence, it can be speculated that the small amount of CTAB may preferentially adsorb on the (010) crystal planes, while the hydrophobic tails inhibit the further growth along *b*-axis to form a nanoplate-like morphology. And it is also beneficial to crystal nucleation process and subsequent crystallization process. With further increase in the amount of CTAB, spherical micelles would form with precursor clusters encapsulated, leading to the formation of aggregates morphology. However, excess CTAB may exert negative effect on the crystallization process, probably due to the micellization effect of CTAB and the competition between CTAB and TPAOH.

Besides, CTAB can also promote the incorporation of Ti in TS-1 framework as discussed in Section 3.1.2. Due to the difficulty in synthesis, the content of framework Ti in TS-1 is typically as low as 2–3 wt %. Strategies to increase the content of framework Ti include desilication treatment followed by post-impregnation of Ti [50], optimization of environmental medium of crystallization process [51], seed-assisted synthesis method, [44] etc. However, these methods have several disadvantages, including long crystallization time and complex multi-step

processes. In this work, addition of appropriate amount of CTAB significantly increase the Ti content to 7.8 wt% (1 C-TS-1). According to literature, it can be speculated that CTAB can slow down the velocity of the hydrolysis of Ti precursors, and form a synchronous hydrolysis process of Ti and Si precursors, which is beneficial to the uniformly distribution of Ti species into the Si species [52]. The accelerated crystallization process also contributes to the incorporation of these Ti species in the framework of TS-1. But excess CTAB may lead to the generation of more extra-framework Ti due to the broken assemble equilibrium.

In summary, by using CTAB as a secondary SDA, we realize the regulation of morphology of TS-1 between nanoplates and aggregates, as well as a significant increase of framework Ti content. It can be expected that the TS-1 nanoplates may exhibit better performance in photocatalysis reactions benefiting from larger exposed surface under light irradiation and more Ti active sites on the surface. Meanwhile, compared with conventional synthesis approaches of zeolite nanoplates or nanosheets which require the use of another reagent like NH<sub>4</sub>F [53] or a special template [38,54], the regulation of morphology by only one key reagent can exclude the influence of residual reagents, which is beneficial to subsequent studies of structure-activity relationships.

### 3.2. Photoelectric chemical properties of xC-TS-1 catalysts

The photocatalytic activity of TS-1 arises from the LMCT photoexcitation between framework Ti and coordinated O, so the optimization of Ti amount and morphology by dual-SDA method may significantly influence the photoelectric chemical properties of xC-TS-1 catalysts. The photocurrent response curves (Fig. 6a) show that 1 C-TS-1 exhibits appreciably higher photocurrent density than other samples, indicating its superior photo-activity. However, the samples with larger external surface area (2 C-TS-1, as shown in Table 2) and higher content of framework Ti (2 C-TS-1 and 5 C-TS-1) which would generate more photo-induced electrons theoretically, exhibit much lower photocurrent density. Obviously, this is caused by the difference in morphologies, considering that the photocurrent density is related to both the amount of photo-generated electrons and charge-separation efficiency. Based on prior literature on advantages of 2D materials in photocatalysis [55], it can be speculated that in the 1 C-TS-1 nanoplates, the shortened *b*-axis (straight channel in MFI structure) would provide a pathway for the charge transfer to the surface, enhancing the utilization of photo-generated charges. On the contrary, the aggregates structure of 2 C-TS-1 and 5 C-TS-1 may provide a large amount of intercrystalline contact interfaces acting as the charge recombination centers, resulting in the low utilization rate of photogenerated charges. The EIS results (Fig. 6b) show that the Nyquist curve of 1 C-TS-1 exhibits the largest radius while those of 2 and 5 C-TS-1 are smaller, furtherly demonstrating the existence of interfacial charge transfer in aggregates structure, which may lead to the recombination of charges at interfaces.

PL spectra was applied to investigate the recombination rate of photogenerated electron-hole pairs. As shown in Fig. 6c, all xC-TS-1 samples exhibit the same emission peak at about 375 nm upon excitation at 250 nm. The fluorescence intensities first increase with the addition of CTAB, and reach the maximum on 1 C-TS-1. It should be pointed out that xC-TS-1 samples are not modified by any metal co-catalysts or semiconductors which would act as electron-trap or form heterojunction to facilitate electron transfer. Therefore, most of the photo-generated electrons would return to the ground state to emit the fluorescence. Together with its high framework Ti content, the 1 C-TS-1 sample exhibits the highest emission peak. However, the fluorescent intensities of 2 and 5 C-TS-1 samples decrease drastically, further demonstrating that the aggregate structure in these two samples causes mainly non-radiative recombination due to spatial separation of charges, and the recombination of charges occurs predominantly at interfaces [56]. The accelerated decay time-resolved PL spectra (Fig. 6d) and the calculated photoelectron lifetimes of each catalyst (Table S1)

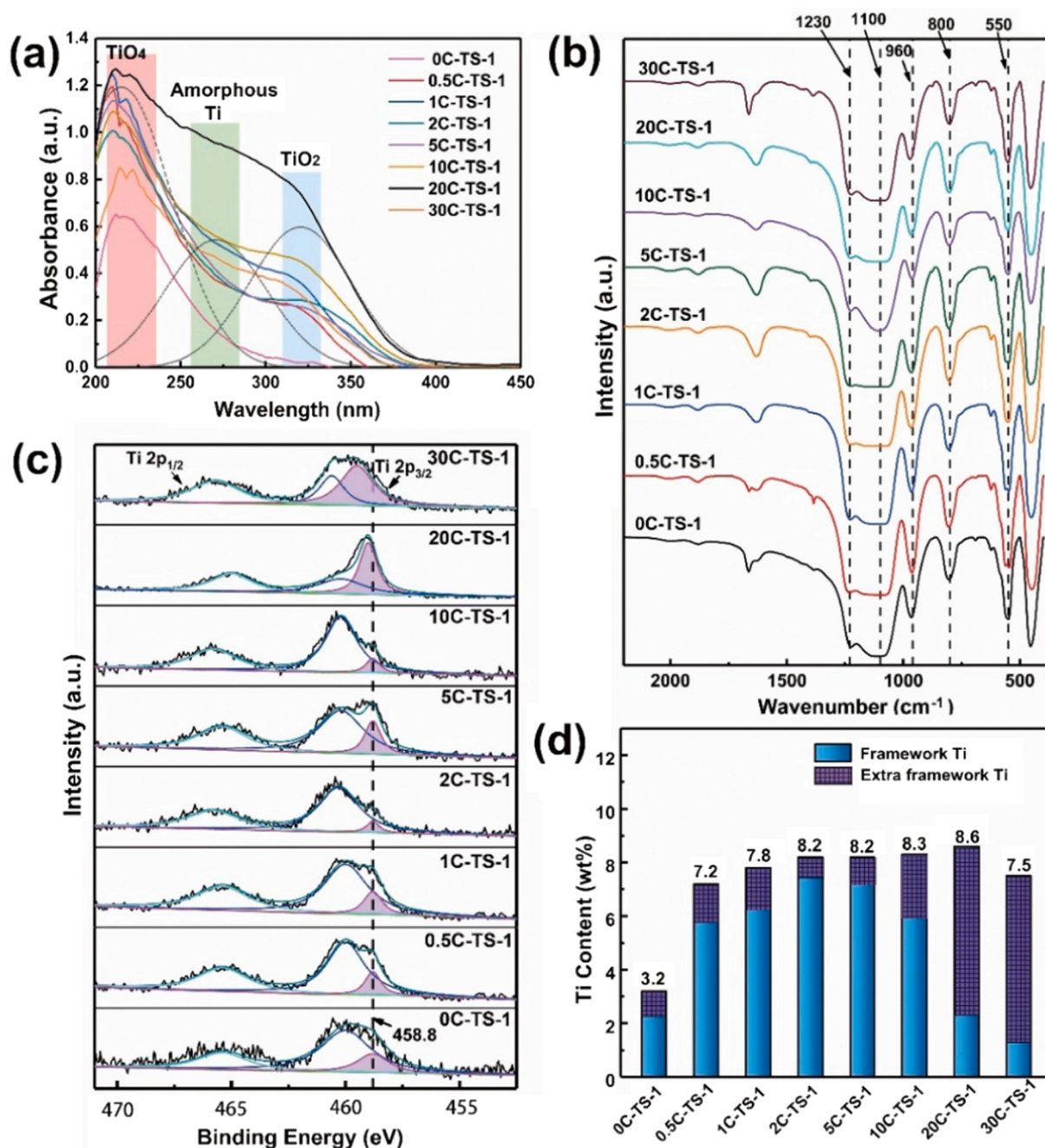


**Fig. 4.** (a) Characterizations of distribution and composition states of Ti species in xC-TS-1 samples: (a) UV-vis spectra, (b) FTIR spectra, (c) XPS spectra and (d) calculated Ti content (from ICP and XPS results).

show that xC-TS-1 samples with low CTAB addition ( $x = 0, 0.5, 1$ ) possess similar photoelectron lifetime within the accuracy errors, illustrating the similar micro-environment of Ti sites in these samples. With further increase of CTAB, the photoelectron lifetime significantly increased to 3.1  $\mu\text{s}$ , indicating the charge transfer caused by the possible formation of heterojunction between TS-1 and excess extra-framework Ti. All these results demonstrate that the regulation of morphology and framework Ti content of xC-TS-1 samples by CTAB as the second SDA would greatly affects the photoactivity.

### 3.3. Performance of xC-TS-1 catalysts in photocatalytic H<sub>2</sub> production and structure-activity relationship

The photocatalytic H<sub>2</sub> production activities of xC-TS-1 catalysts were

evaluated in aqueous methanol solution (molar ratio of CH<sub>3</sub>OH/H<sub>2</sub>O = 1:2), as shown in Fig. 7a. Catalysts synthesized with addition of a small amount of CTAB exhibit significantly enhanced activities (10.7 mmol·g<sup>-1</sup>·h<sup>-1</sup> on optimal 1 C-TS-1 catalyst) compared with the benchmark 0 C-TS-1, while aggregate-like catalysts (2 and 5 C-TS-1) exhibit sharply decreased activities. Based on the photoelectric test and photocatalysis performance, the structure-activity relationship of TS-1 in photocatalysis can be concluded. The Ti-rich nanoplate-like TS-1 could generate more photoelectrons under irradiation, and the photoelectrons could remain to the most extent to participate in the catalytic reactions benefiting from its nanoplate-like morphology, hence exhibits excellent activity. However, aggregate-like TS-1 will generate a large number of intercrystalline interfaces, leading to the recombination of photo-induced charges and decrease of photoactivities. Besides, with



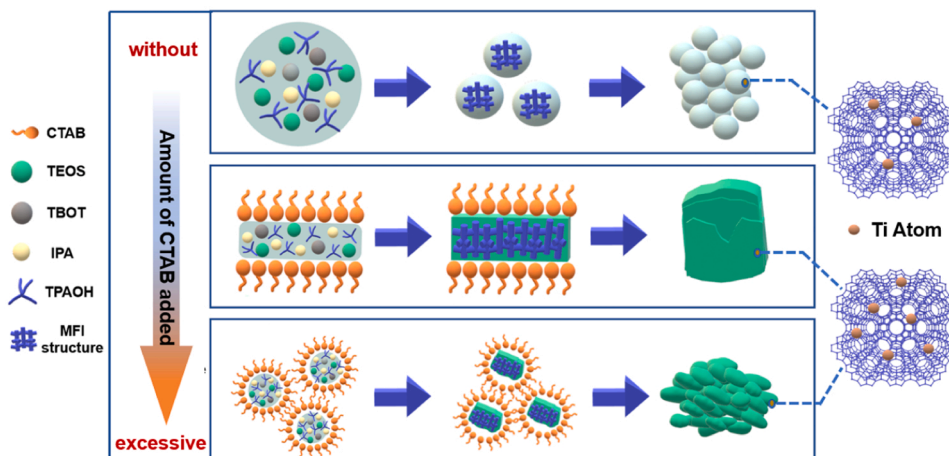


Fig. 5. Schematic illustration of the synthesis mechanism for xC-TS-1 samples with addition of different amount of CTAB.

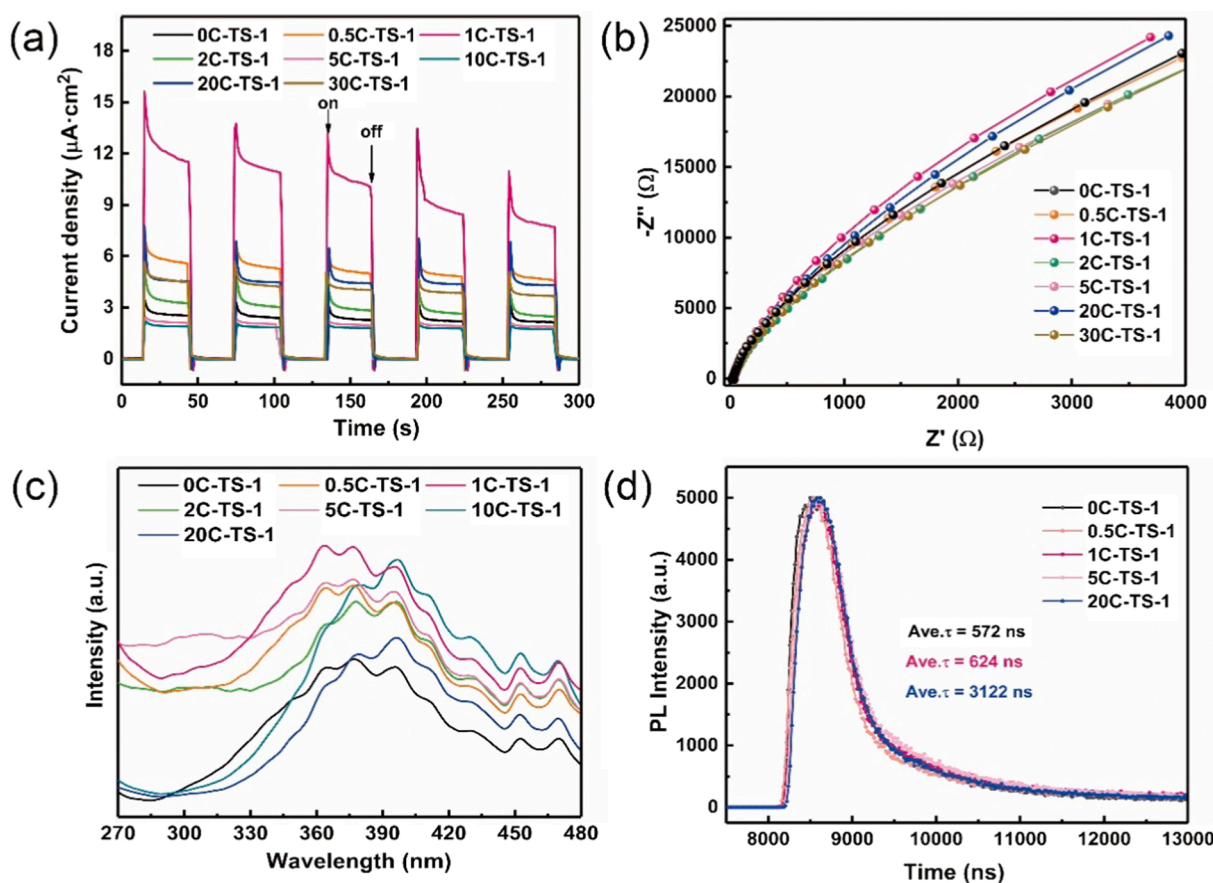


Fig. 6. (a) Transient photocurrent response, (b) EIS Nyquist plots, (c) PL spectra and (d) Time-resolved PL spectra of xC-TS-1 catalysts.

further increase in the amount of CTAB, the activities of the synthesized catalysts increase slightly (peak at 20 C-TS-1) due to the formation of heterojunction structure between TS-1 and excess extra-framework Ti, as can be demonstrated by the increased photocurrent density and higher carrier lifetime (Fig. 6a and d), and then decrease significantly due to the low content of framework Ti and low relative crystallinity. It is worth noting that HCHO was detected as the main oxidation product of  $\text{CH}_3\text{OH}$  on most xC-TS-1 catalysts (Fig. S4) and no  $\text{O}_2$  was detected, demonstrating the advantage on product selectivity of TS-1 as single-site heterogeneous catalyst, and suggesting that  $\text{CH}_3\text{OH}$  may be the main reactant and  $\text{H}_2$  source, rather than  $\text{H}_2\text{O}$ . The reaction mechanism will

be discussed in Section 3.4 in detail.

Due to the low ability for water splitting of TS-1 [57],  $\text{CH}_3\text{OH}$  was used as sacrificial agent in the initial experimental design, and the optimal proportion of reaction solution was investigated on optimal 1 C-TS-1. As shown in Fig. 7b, the  $\text{H}_2$  yield exhibits first an increasing trend and then decrease with increasing the molar ratio of  $\text{CH}_3\text{OH}/\text{H}_2\text{O}$ , and reaches the highest value when the molar ratio of  $\text{CH}_3\text{OH}$  to  $\text{H}_2\text{O}$  is 1:2. This result suggests a synergistic function between  $\text{CH}_3\text{OH}$  and  $\text{H}_2\text{O}$ , and this will be discussed in Section 3.4 in detail.

The efficiency of the photocatalytic reaction on different Ti-based photocatalysts was evaluated and compared in terms of  $\text{H}_2$  production



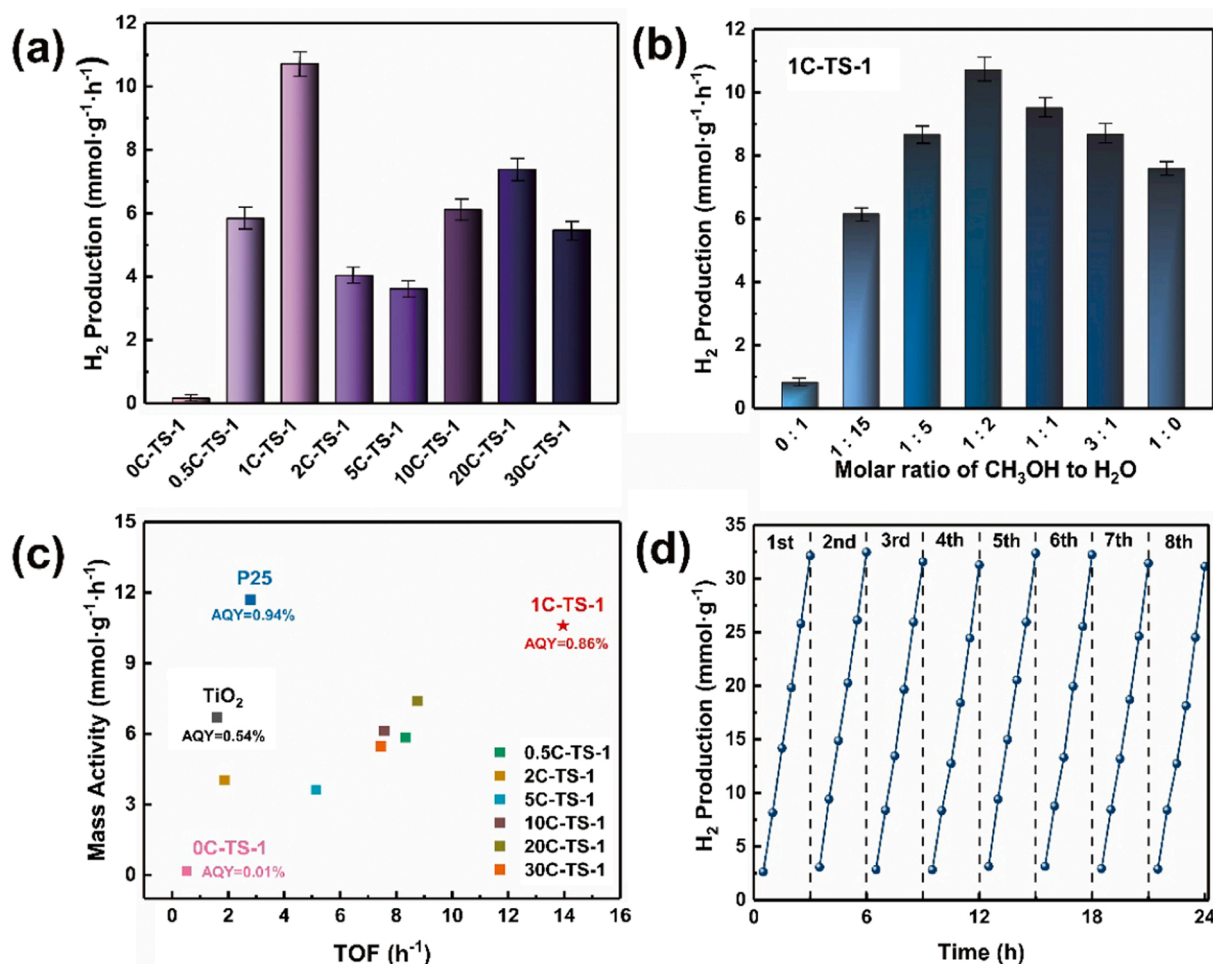


**Fig. 7.** Photocatalytic performance of xC-TS-1 catalysts: (a) Hydrogen production rates of xC-TS-1 samples (molar ratio of CH<sub>3</sub>OH to H<sub>2</sub>O = 1:2), (b) Hydrogen production rates of optimal 1C-TS-1 under different reactant concentrations, (c) Comparison of the photocatalytic performance of xC-TS-1 catalysts with other Ti-based photocatalysts, (d) Durability tests of the optimal 1C-TS-1 photocatalyst (3 h per cycle). Error bars represent the means  $\pm$  s.d. of three independent experiments. Reaction conditions: T = 298 K, 20 mg of catalyst, 30 mL of aqueous methanol solution, 500 W mercury lamp.

rates, apparent quantum yield (AQY) and the turnover frequency (TOF, per mole Ti), as shown in Fig. 7c. The most representative studies of photocatalytic H<sub>2</sub> production on different Ti-based photocatalysts in the last five years are listed in Table S2. Most of xC-TS-1 catalysts possess higher TOF value than TiO<sub>2</sub> semiconductor-based catalysts, demonstrating the high activity of 4-coordinated Ti. Besides, the significantly decreased TOF on 2, 5, 10 C-TS-1 also indicates the advantage of nanoplate-like morphology in photocatalysis over aggregates morphology. As pointed out before, despite the high activity of framework Ti sites, the low Ti content in TS-1 leads to the low activity per unit mass compared to other Ti-based photocatalysts [58]. However, in this work, 1C-TS-1 possesses higher H<sub>2</sub> production rate and AQY than anatase TiO<sub>2</sub>, and can be comparable to commercial P25.

Besides the high catalytic activity, no decrease of H<sub>2</sub> production rate was observed (Fig. 7d) on 1C-TS-1 after eight cycles (24 h in total), confirming the excellent durability and stability of TS-1 in photocatalysis. In our exploring experiments, 1C-TS-1 loaded with Pt, Fe<sub>2</sub>O<sub>3</sub> and Cu (Pt/1C-TS-1, Fe<sub>2</sub>O<sub>3</sub>/1C-TS-1 and Cu/1C-TS-1) exhibit excellent performance in photocatalytic H<sub>2</sub> production, photo-Fenton degradation of methylene blue and photocatalytic CO<sub>2</sub> reduction respectively (Fig. S5, Fig. S6 and Fig. S7). More importantly, the photoresponsive range of 1C-TS-1 can be broadened to the visible light range to different extents, depending on the properties of different cocatalysts loaded (Fig. S8). Therefore, considering the advantages of facile synthesis, high activity, high product selectivity, high stability, and other possible

advantages derived from its porous structure, we believe that the Ti-rich nanoplate-like 1C-TS-1 optimized by the dual-SDA method shows great potential for the commercialization as a new generation of photocatalyst, or as an excellent support for other photocatalysts.

#### 3.4. Reaction mechanism and actual active sites of TS-1 in photocatalysis

*In-situ* DRIFTS was performed to probe the reaction pathway. Fig. 8 presents the *in-situ* DRIFTS spectra with increased irradiation times on the optimal 1C-TS-1 catalyst. The positions of the main peaks and corresponding groups are noted in the diagram and are summarized in Table S3. In the presence of methanol and water vapor without light, a strong Ti–OH peak was detected, suggesting the dissociative adsorption of H<sub>2</sub>O on Ti. The weak peak of Si–OH also suggests the possible hydrolysis of Ti–O–Si [59]. Besides, the peaks of methanol adsorption on TS-1 surface was detected, and the intensities of CH<sub>3</sub>OH and •OCH<sub>3</sub> peaks decline gradually and that of HCHO peaks increase gradually with the irradiation time, while only very weak HCOO• peaks and no other intermediates were observed, indicating the highly selective production of HCHO. Similarly, the *in-situ* DRIFTS spectra were also obtained on 0C-TS-1 catalyst as provided in Fig. S9. It is apparent that very similar reaction intermediates were detected on both catalysts, suggesting the same active sites and similar reaction process occurred, and the differences in peak intensities are caused by the difference in Ti content. In summary, the *in-situ* DRIFTS results indicate that both H<sub>2</sub>O and CH<sub>3</sub>OH

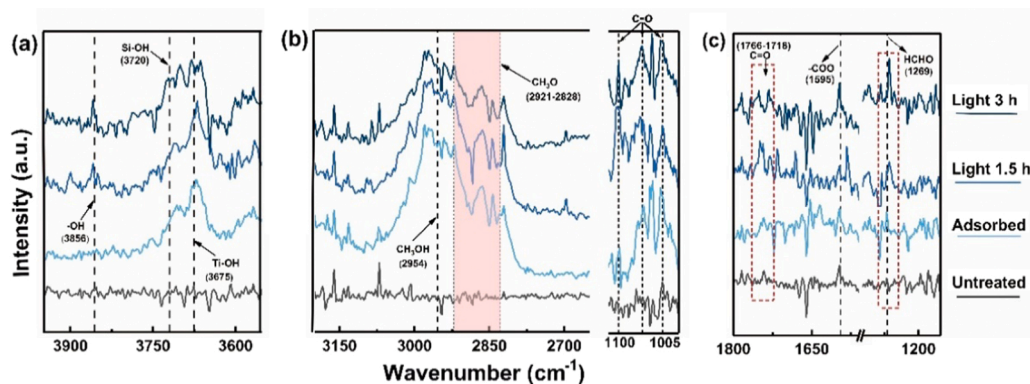


Fig. 8. In-situ DRIFTS spectra of  $\text{CH}_3\text{OH}/\text{H}_2\text{O}$  adsorption and reaction on 1 C-TS-1 catalyst.

participated in the surface adsorption and reactions on TS-1.

The real photocatalysis active sites of TS-1 need to be explored further. Most of the previous works [24,60] proposed that the photocatalysis mechanism on TS-1 is based on the photo-induced LMCT process in  $\text{Ti}^{4+}-\text{O}^{2-}$  units, leading to the formation of  $\text{Ti}^{3+}$  as the reduction sites and  $\text{O}^\cdot$  as the oxidation sites. However, we have doubts about this opinion because of the relatively difficult adsorption of reactant molecules on saturated coordinated O atoms. Therefore, we calculated the adsorption energies of  $\text{CH}_3\text{OH}$  and  $\text{H}_2\text{O}$  on Ti, O, and Si sites, respectively (Table S4). It is found that both  $\text{CH}_3\text{OH}$  and  $\text{H}_2\text{O}$  are hard to adsorb on O sites, and are most preferentially to adsorb on Ti sites, indicating that Ti sites are the real reaction sites for  $\text{CH}_3\text{OH}$  and  $\text{H}_2\text{O}$ , instead of being oxidized on O sites. It is known that 4-coordinated  $\text{Ti}^{4+}$  in TS-1 is not saturated coordinated (tends to form 6-coordinated structure) [61]. As a result, this type of defect in the electronic

structure exhibits an electrophilic property, resulting in a strong intermolecular interaction force towards the reactant molecules, especially the O atoms in  $\text{CH}_3\text{OH}$  and  $\text{H}_2\text{O}$ . We further calculated the free energies for  $\text{H}_2$  evolution from  $\text{CH}_3\text{OH}$  and  $\text{H}_2\text{O}$  on Ti sites. Fig. 9a indicates that  $\text{H}_2\text{O}$  is readily adsorbed and dissociated on Ti sites, consistent with the abundant Ti-OH in in-situ DRIFTS results. However, it is hard to generate  $\text{H}_2$  due to the extremely high activation energy, as well as lack of  $^*\text{H}$  source. It is known that two electrons are needed in  $\text{H}_2\text{O}$  splitting. Therefore,  $\text{H}_2\text{O}$  splitting may not occur on TS-1 because only one electron can be generated by LMCT process in a single Ti site. In the pathway of  $\text{CH}_3\text{OH}$  conversion to  $\text{HCHO}$  and  $\text{H}_2$ , it can be seen that  $\text{CH}_3\text{OH}$  is more prone to adsorption and dissociation on Ti sites than  $\text{H}_2\text{O}$ , and the adjacent O can accept the generated  $^*\text{H}$ . Then it overcomes 1.03 eV to break the C-H bond (Step III to IV) and provides another H to generate  $\text{H}_2$ , and 0.80 eV to  $\text{HCHO}$  desorption (Step IV to V). Obviously, the

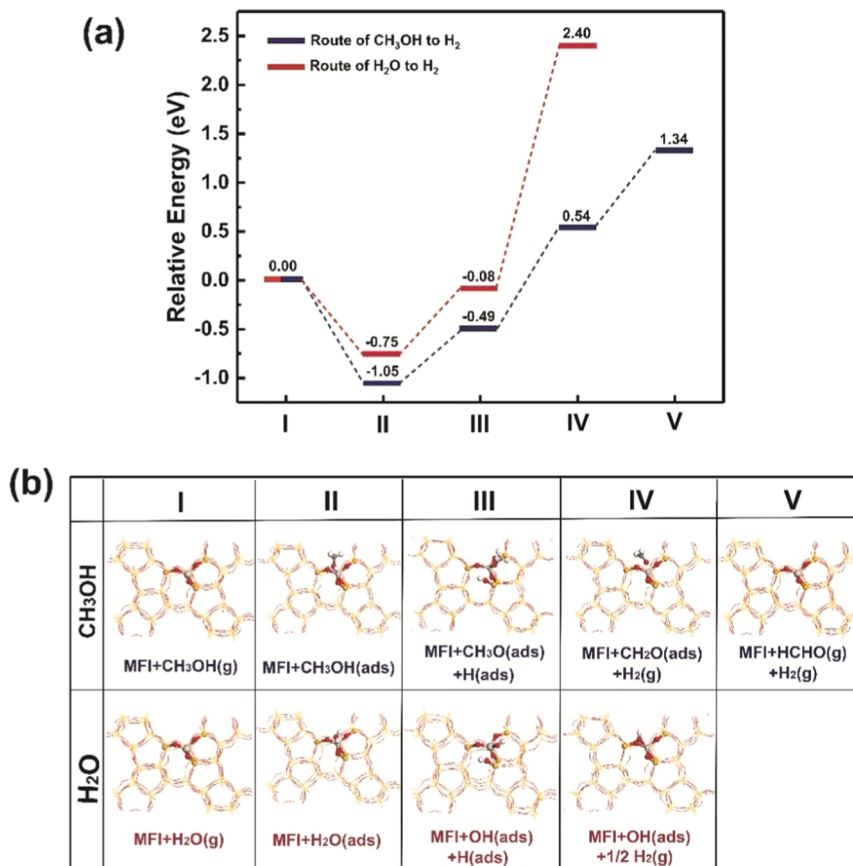


Fig. 9. (a) Free energies and (b) structural models of intermediates for  $\text{H}_2$  evolution from  $\text{CH}_3\text{OH}$  and  $\text{H}_2\text{O}$  on Ti sites.

required energy can be provided by light irradiation and light-induced electrons by LMCT process. Based on the foregoing results, we speculate that  $\text{CH}_3\text{OH}$  are the  $\text{H}_2$  source, and the  $\text{Ti}-\text{O}$  in TS-1 would function as a whole to serve as the photocatalytic active site, in which the Ti acts as the main adsorption and activation sites for reactants, and adjacent O can accept reaction intermediate like  $^*\text{H}$ . This conclusion can be supported by the most up-to-date study of Ti-MOFs photocatalysts recently, in which it was proposed that  $\text{Ti}-\text{O}$  in Ti-based MOFs would function as a whole to serve as the photocatalysis active site [62]. Besides, it can be speculated that if  $\text{Ti}-\text{O}$  is modified by metal or semiconductors, the light-induced electrons may transfer to these electron traps to generate separated oxidation and reduction sites (as proposed in Fig. S10), leading to higher photocatalysis performance.

In our experiment, as shown in Fig. 7b, the  $\text{H}_2$  yield achieved on the optimal 1 C-TS-1 catalyst greatly increased when  $\text{CH}_3\text{OH}$  was added in the reaction, and the high  $\text{H}_2$  yield can be achieved over a wide  $\text{CH}_3\text{OH}$  concentration range (molar ratio of  $\text{CH}_3\text{OH}$  to  $\text{H}_2\text{O}$  from 1:15–1:0), indicating that  $\text{CH}_3\text{OH}$  was the main  $\text{H}_2$  source, consistent with our calculated results. However, the highest activity was not achieved at the highest  $\text{CH}_3\text{OH}$  concentration, but there exists an optimal ratio (molar ratio of  $\text{CH}_3\text{OH}$  to  $\text{H}_2\text{O}$  = 1:2), suggesting a promotion effect of  $\text{H}_2\text{O}$  to the photoactivity of TS-1. As aforementioned, a large number of  $\text{Ti}-\text{OH}$  are generated in the presence of  $\text{H}_2\text{O}$  and  $\text{CH}_3\text{OH}$  (in-situ DRIFTS results in Fig. 8), including  $\text{Ti}(\text{OH})-\text{O}_4$  originated from the adsorption and dissociation of  $\text{H}_2\text{O}$  on Ti sites, or  $\text{Ti}(\text{OH})-\text{O}_3$  originated from the hydrolysis of  $\text{Ti}-\text{O}-\text{Si}$ . Therefore, we speculate that  $\text{Ti}-\text{OH}$  may be the key intermediate responsible for the high  $\text{H}_2$  yields. First, in order to probe whether the generation of  $\text{Ti}-\text{OH}$  would change the charge excitation process, we established the corresponding model of hydroxylated Ti and investigated the highest occupied molecular orbital (HOMO) and the lowest unoccupied molecular orbital (LUMO). As shown in Fig. 10, the LUMO can be correlated with the tetrahedral  $\text{Ti}^{4+} \text{dz}^2$  state, consistent with the unhydroxylated  $\text{Ti}-\text{O}_4$  units in benchmark TS-1 [63]. However, the location of HOMO greatly changes to the O 2p orbitals in the  $\text{Ti}-\text{OH}$  hydroxyl, in contrast to the HOMO of benchmark TS-1 model which is comprised of the O 2p orbitals in  $\text{Si}-\text{OH}$  hydroxyl [63]. Therefore, the close spatial distance between the location of HOMO and LUMO apparently suggests a higher photoexcitation activity on hydroxylated TS-1 than that on benchmark TS-1.

We furtherly calculated the free energies for the whole pathway of  $\text{H}_2$  evolution from  $\text{CH}_3\text{OH}$  on the hydroxylated Ti sites. As shown in Fig. 11a,  $\text{Ti}-\text{OH}$  exhibits extremely strong adsorption capacity for  $\text{CH}_3\text{OH}$  ( $E_{\text{ads}} = -1.34$  eV, Step III to IV) compared with unhydroxylated

Ti sites ( $E_{\text{ads}} = -1.05$  eV, Fig. 9a). Subsequently, the adsorbed  $\text{CH}_3\text{OH}$  also tends to replace the  $\text{H}_2\text{O}$  molecule, leading to the dissociation of  $\text{CH}_3\text{OH}$  to  $^*\text{OCH}_3$ , and this process is thermodynamically favored (Step III to VII). Then the following processes include the cleavage of C–H bond, the generation of  $\text{H}_2$ , and the desorption of  $\text{HCHO}$ . These results once again demonstrate that  $\text{CH}_3\text{OH}$  is the source of  $\text{H}_2$ , and more importantly reveal the promotion mechanism of  $\text{H}_2\text{O}$  to  $\text{H}_2$  production from  $\text{CH}_3\text{OH}$ .

Taking into considerations of all the experimental and DFT calculation results and analysis presented above, the mechanism of photocatalytic  $\text{H}_2$  production on TS-1 through  $\text{CH}_3\text{OH}$  dehydrogenation which is promoted by the presence of  $\text{H}_2\text{O}$  is proposed as displayed in Fig. 11b. In aqueous solution, hydrolysis of Ti sites or adsorption of  $\text{H}_2\text{O}$  may take place, leading to the formation of hydroxylated  $\text{Ti}(\text{OH})-\text{O}_3$  or  $\text{Ti}(\text{OH})-\text{O}_4$  structures. The hydroxylated Ti sites possess higher photoactivity due to the change in the location of HOMO and LUMO. Meanwhile,  $\text{CH}_3\text{OH}$  would be more prone to adsorption and activation on  $\text{Ti}-\text{OH}$ . Under UV irradiation, the electrons generated by LMCT process would lead to the cleavage of C–H bonds, and the generation of  $\text{H}_2$  and  $\text{HCHO}$  via the  $\text{CH}_3\text{OH}$  dehydrogenation reaction. It is worth noting that the whole photocatalysis reaction takes place on the  $\text{Ti}-\text{O}$  sites, rather than separated reduction sites and oxidation sites on Ti and O, respectively.

#### 4. Conclusions

In this work, we achieved the optimization of TS-1 in both the morphology and the content of framework Ti by a simple dual-structure directing agent method. Optimal 1 C-TS-1 catalyst exhibits significantly enhanced activity in photocatalytic  $\text{H}_2$  production reactions in aqueous methanol solutions, particularly the activity exceeds that of anatase  $\text{TiO}_2$ , and is comparable to commercial P25. The enhanced performance is not only owing to the increased content of framework Ti, but also owing to the nanoplate morphology. The photogenerated electrons in nanoplate-like TS-1 would be largely retained to precipitate in photocatalysis reactions, benefiting from the large crystal plane, as well as shortened pathway of electrons transfer along *b*-axis. However, TS-1 with aggregates structure would generate a large amount of intracrystalline interfaces, leading to the recombination of photo-induced charges and decrease of photoactivities. The aforementioned structure-activity relationship of TS-1 in photocatalysis may be proposed for the first time, which is quite different with that in thermal-catalysis, in which TS-1 aggregates with high specific area and abundant mesopores is more favorable.

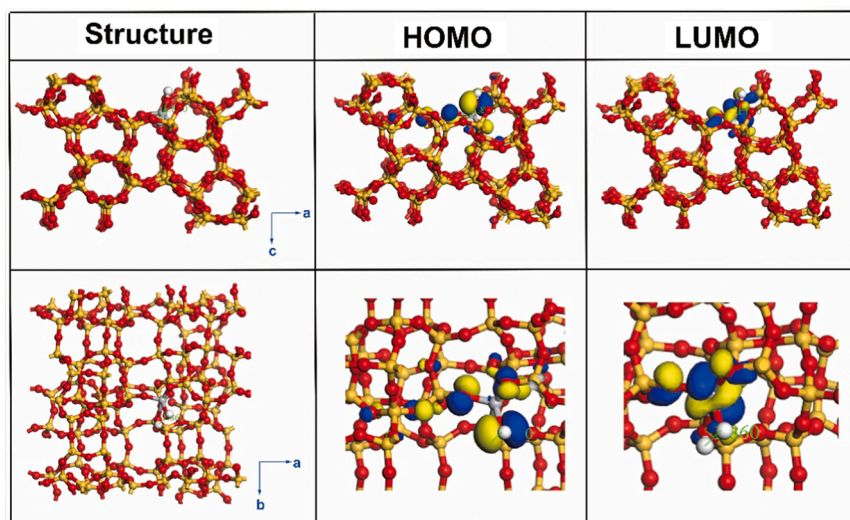


**Fig. 10.** HOMO and LUMO of TS-1 model with hydroxylated Ti sites. The yellow and blue colors represent the possible distributions of HOMO and LUMO on different atoms.



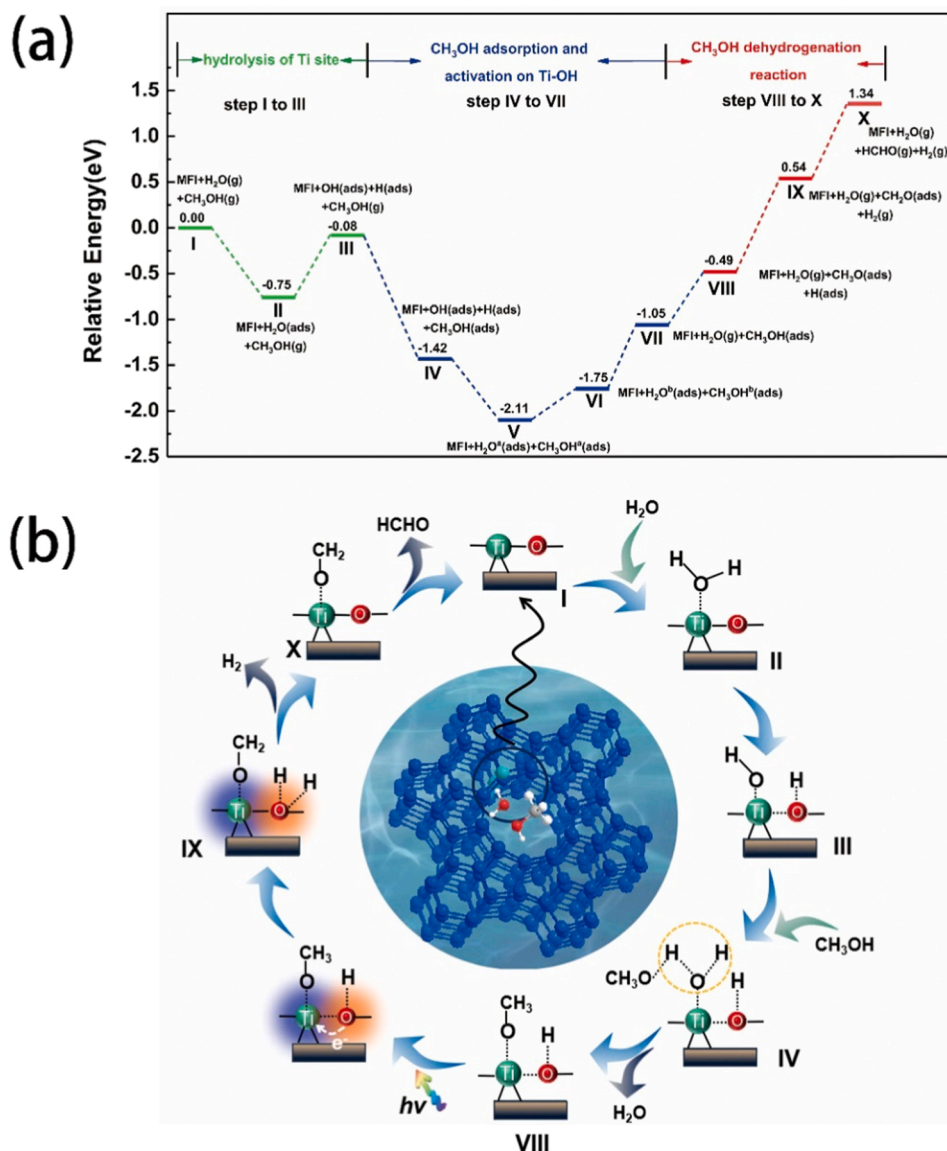


**Fig. 11.** (a) Free energies for the whole pathway of  $\text{H}_2$  evolution from  $\text{CH}_3\text{OH}$  on hydroxylated Ti sites, (b) Schematic illustration for the mechanism of photocatalytic  $\text{H}_2$  evolution from  $\text{CH}_3\text{OH}$  over TS-1 catalyst (in the presence of  $\text{H}_2\text{O}$ ).

The reaction mechanism and actual photocatalytic active sites in TS-1 are proposed as below. Ti–O in TS-1 may function as a whole to serve as the photocatalysis active site, in which Ti possess strong capability to adsorb and activate reactant molecules, while coordinated O sites could accept reaction intermediates. On such Ti–O sites,  $\text{H}_2$  are mainly generated by  $\text{CH}_3\text{OH}$  dehydrogenation owing to the strong adsorption of  $\text{CH}_3\text{OH}$  on Ti, while  $\text{H}_2\text{O}$  splitting is unlikely to occur due to the high reaction activation energy and the lack of  $\cdot\text{H}$ . However, it is also found that  $\text{H}_2\text{O}$  has a promotion effect on the photocatalytic performance. The hydroxylated Ti formed in the presence of  $\text{H}_2\text{O}$ , possess higher photoactivity due to the change in location of HOMO and LUMO. Meanwhile,  $\text{CH}_3\text{OH}$  would be more prone to adsorption and activation on Ti–OH.

In summary, we refine the theory of TS-1 as photocatalyst from aspect of structure-activity relationship and actual active sites. The Ti-rich TS-1 nanoplates catalysts could be a potential commercial photocatalytic material.

#### CRediT authorship contribution statement

**Pengxian Tao:** Conceptualization, Data curation, Formal analysis,

Investigation, Methodology, Writing – original draft. **Xiao Wang:** Formal analysis, Conceptualization, Methodology, Writing – review & editing, Funding acquisition. **Qiao Zhao:** DFT calculations, Software – Validation, Methodology, Resources, Writing – review & editing, Funding acquisition. **Hongxia Guo:** Writing – review & editing. **Li Liu:** Conceptualization, Supervision. **Xiwei Qi:** Writing – review & editing. **Wenquan Cui:** Conceptualization, Project administration, Supervision, Funding acquisition.

#### Declaration of Competing Interest

The authors declare that they have no known competing financial interests or personal relationships that could have appeared to influence the work reported in this paper.

#### Data availability

Data will be made available on request.



## Acknowledgements

This work was supported by the National Natural Science Foundation of China (Grant No. 21908052 and 22108200); the Key Program of Natural Science Foundation of Hebei Province (Grant No. B2020209017); the Project of Science and Technology Innovation Team, Tangshan (NO. 20130203D); the Natural Science Foundation of Zhejiang Province (Grant No. LQ22B060013); and the Science and Technology Project of Hebei Education Department (Grant No. QN2021113).

## Appendix A. Supporting information

Supplementary data associated with this article can be found in the online version at doi:10.1016/j.apcatb.2023.122392.

## References

- [1] H. Wang, X. Li, X. Zhao, C. Li, X. Song, P. Zhang, P. Huo, X. Li, A review on heterogeneous photocatalysis for environmental remediation: from semiconductors to modification strategies, *Chin. J. Catal.* 43 (2022) 178–214, [https://doi.org/10.1016/S1872-2067\(21\)63910-4](https://doi.org/10.1016/S1872-2067(21)63910-4).
- [2] L. Wang, C.S. Tsang, W. Liu, X. Zhang, K. Zhang, E. Ha, W.M. Kwok, J.H. Park, L.Y. S. Lee, K.Y. Wong, Disordered layers on WO<sub>3</sub> nanoparticles enable photochemical generation of hydrogen from water, *J. Mater. Chem. A* 7 (2019) 221–227, <https://doi.org/10.1039/c8ta09446b>.
- [3] M. Xu, D. Li, K. Sun, L. Jiao, C. Xie, C. Ding, H.L. Jiang, Interfacial microenvironment modulation boosting electron transfer between metal nanoparticles and MOFs for enhanced photocatalysis, *Angew. Chem. Int. Ed.* 60 (2021) 16372–16376, <https://doi.org/10.1002/anie.202104219>.
- [4] X. Zhao, L. Wang, Y. Pei, Single metal atom catalyst supported on g-C<sub>3</sub>N<sub>4</sub> for formic acid dehydrogenation: a combining density functional theory and machine learning study, *J. Phys. Chem. C* 125 (2021) 22513–22521, <https://doi.org/10.1021/acs.jpcc.1c05734>.
- [5] X. Yang, D. Wang, Photocatalysis: from fundamental principles to materials and applications, *ACS Appl. Energy Mater.* 1 (2018) 6657–6693, <https://doi.org/10.1021/acsaem.8b01345>.
- [6] J. Zhang, Q. Xu, Z. Feng, M. Li, C. Li, Importance of the relationship between surface phases and photocatalytic activity of TiO<sub>2</sub>, *Angew. Chem. Int. Ed.* 47 (2008) 1766–1769, <https://doi.org/10.1002/anie.200704788>.
- [7] W. Weng, J. Guo, The effect of enantioselective chiral covalent organic frameworks and cysteine sacrificial donors on photocatalytic hydrogen evolution, *Nat. Commun.* 13 (2022) 5768, <https://doi.org/10.1038/s41467-022-33501-8>.
- [8] J. Low, J. Yu, M. Jaroniec, S. Wageh, A.A. Al-Ghamdi, Heterojunction photocatalysts, *Adv. Mater.* 29 (2017), 1601694, <https://doi.org/10.1002/adma.201601694>.
- [9] X. Hou, L. Cui, H. Du, L. Gu, Z. Li, Y. Yuan, Lowering the schottky barrier of g-C<sub>3</sub>N<sub>4</sub>/Carbon graphite heterostructure by N-doping for increased photocatalytic hydrogen generation, *Appl. Catal. B Environ.* 278 (2020), 119253, <https://doi.org/10.1016/j.apcatb.2020.119253>.
- [10] Y. Wang, A. Vogel, M. Sachs, R.S. Sprick, L. Wilbraham, S.J.A. Moniz, R. Godin, M. A. Zwienerburg, J.R. Durrant, A.I. Cooper, J. Tang, Current understanding and challenges of solar-driven hydrogen generation using polymeric photocatalysts, *Nat. Energy* 4 (2019) 746–760, <https://doi.org/10.1038/s41560-019-0456-5>.
- [11] Q. Zhu, Q. Xu, M. Du, X. Zeng, G. Zhong, B. Qiu, J. Zhang, Recent progress of metal sulfide photocatalysts for solar energy conversion, *Adv. Mater.* (2022), 2202929, <https://doi.org/10.1002/adma.202202929>.
- [12] M. Anpo, J.M. Thomas, Single-site photocatalytic solids for the decomposition of undesirable molecules, *Chem. Commun.* (2006) 3273–3278, <https://doi.org/10.1039/b606738g>.
- [13] H. Yamashita, K. Mori, Y. Kuwahara, T. Kamegawa, M. Wen, P. Verma, M. Che, Single-site and nano-confined photocatalysts designed in porous materials for environmental uses and solar fuels, *Chem. Soc. Rev.* 47 (2018) 8072–8096, <https://doi.org/10.1039/c8cs00341f>.
- [14] A. Fermi, A. Gualandi, G. Bergamini, P.G. Cozzi, Shining light on Ti<sup>IV</sup> complexes: exceptional tools for metallaphotoredox catalysis, *Eur. J. Org. Chem.* 45 (2020) 6955–6965, <https://doi.org/10.1002/ejoc.202000966>.
- [15] D.C. Hurum, K.A. Gray, T. Rajh, M.C. Thurnauer, Recombination pathways in the Degussa P25 formulation of TiO<sub>2</sub>: surface versus lattice mechanisms, *J. Phys. Chem. B* 109 (2005) 977–980, <https://doi.org/10.1021/jp045395d>.
- [16] G. Li, N.M. Dimitrijevic, L. Chen, J.M. Nichols, T. Rajh, K.A. Gray, The important role of tetrahedral Ti<sup>4+</sup> sites in the phase transformation and photocatalytic activity of TiO<sub>2</sub> nanocomposites, *J. Am. Chem. Soc.* 130 (2008) 5402–5403, <https://doi.org/10.1021/ja711118u>.
- [17] H. Yamashita, Y. Fujii, Y. Ichihashi, S.G. Zhang, K. Ikeue, D.R. Park, K. Koyano, T. Tatsumi, M. Anpo, Selective formation of CH<sub>3</sub>OH in the photocatalytic reduction of CO<sub>2</sub> with H<sub>2</sub>O on titanium oxides highly dispersed within zeolites and mesoporous molecular sieves, *Catal. Today* 45 (1998) 221–227, [https://doi.org/10.1016/S0920-5861\(98\)00219-3](https://doi.org/10.1016/S0920-5861(98)00219-3).
- [18] S.L. Suib, J. Prech, J. Čejka, Y. Kuwahara, K. Mori, H. Yamashita, Some novel porous materials for selective catalytic oxidations, *Mater. Today* 32 (2020) 244–259, <https://doi.org/10.1016/j.mattod.2019.06.008>.
- [19] R. Bai, Y. Song, R. Bai, J. Yu, Creation of hierarchical titanasilicate TS-1 zeolites, *Adv. Mater. Interfaces* 8 (2020), 2001095, <https://doi.org/10.1002/admi.202001095>.
- [20] M. Tamura, W. Chaikittisilp, T. Yokoi, T. Okubo, Incorporation process of Ti species into the framework of MFI type zeolite, *Microporous Mesoporous Mater.* 112 (2008) 202–210, <https://doi.org/10.1016/j.micromeso.2007.09.044>.
- [21] Z. Zhao, D.G. Cheng, F. Chen, X. Zhan, Hierarchical porous TS-1/Pd/CdS catalysts for enhanced photocatalytic hydrogen evolution, *Int. J. Hydrog. Energ.* 45 (2020) 33532–33542, <https://doi.org/10.1016/j.ijhydene.2020.09.099>.
- [22] M. Anpo, Photocatalytic reduction of CO<sub>2</sub> with H<sub>2</sub>O on highly dispersed Ti-oxide catalysts as a model of artificial photosynthesis, *J. CO<sub>2</sub> Util.* 1 (2013) 8–17, <https://doi.org/10.1016/j.jcou.2013.03.005>.
- [23] Y. Tong, L. Chen, S. Ning, N. Tong, Z. Zhang, H. Lin, F. Li, X. Wang, Photocatalytic reduction of CO<sub>2</sub> to CO over the Ti-highly dispersed HZSM-5 zeolite containing Fe, *Appl. Catal. B Environ.* 203 (2017) 725–730, <https://doi.org/10.1016/j.apcatb.2016.10.065>.
- [24] M. Anpo, T.H. Kim, M. Matsuoka, The design of Ti-, V-, Cr-oxide single-site catalysts within zeolite frameworks and their photocatalytic reactivity for the decomposition of undesirable molecules-The role of their excited states and reaction mechanisms, *Catal. Today* 142 (2009) 114–124, <https://doi.org/10.1016/j.cattod.2008.11.006>.
- [25] X. Yu, L. Yang, Y. Xuan, X.L. Liu, K. Zhang, Solar-driven low-temperature reforming of methanol into hydrogen via synergetic photo- and thermocatalysis, *Nano Energy* 84 (2021), 105953, <https://doi.org/10.1016/j.nanoen.2021.105953>.
- [26] J. Zhao, R. Shi, Z. Li, C. Zhou, T. Zhang, How to make use of methanol in green catalytic hydrogen production, *Nano Sel.* 1 (2020) 12–29, <https://doi.org/10.1002/nano.202000010>.
- [27] H. Xin, J. Zhao, S. Xu, J. Li, W. Zhang, X. Guo, E.J.M. Hensen, Q. Yang, C. Li, Enhanced catalytic oxidation by hierarchically structured TS-1 zeolite, *J. Phys. Chem. C* 114 (2010) 6553–6559, <https://doi.org/10.1021/jp912112h>.
- [28] S. Du, H.M. Chen, H.X. Shen, J. Chen, C.P. Li, M. Du, Hierarchically nanoporous TS-1 zeolites for catalytic oxidation desulfurization of liquid fuels, *ACS Appl. Nano Mater.* 3 (2020) 9393–9400, <https://doi.org/10.1021/acsaanm.0c02017>.
- [29] Q. Lv, G. Li, H. Lu, W. Cai, H. Huang, C. Cheng, Preparation of magnetic zeolite γ-Fe<sub>2</sub>O<sub>3</sub>/TS-1 with core/shell structure and application in photocatalytic degradation, *Microporous Mesoporous Mater.* 203 (2015) 202–207, <https://doi.org/10.1016/j.micromeso.2014.10.040>.
- [30] B. Delley, An all-electron numerical method for solving the local density functional for polyatomic molecules, *J. Chem. Phys.* 92 (1990) 508, <https://doi.org/10.1063/1.458452>.
- [31] B. Delley, From molecules to solids with the DMol<sup>3</sup> approach, *J. Chem. Phys.* 113 (2000) 7756–7764, <https://doi.org/10.1063/1.1316015>.
- [32] B. Delley, Hardness conserving semilocal pseudopotentials, *Phys. Rev. B* 66 (2002), 155125, <https://doi.org/10.1103/PhysRevB.66.155125>.
- [33] J. Dong, H. Zhu, Y. Xiang, Y. Wang, P. An, Y. Gong, Y. Liang, L. Qiu, A. Zheng, X. Peng, M. Lin, G. Xu, Z. Guo, D. Chen, Toward a unified identification of Ti location in the MFI framework of high-Ti-Loaded TS-1: combined EXAFS, XANES, and DFT study, *J. Phys. Chem. C* 120 (2016) 20114–20124, <https://doi.org/10.1021/acs.jpcc.6b05087>.
- [34] Y. Shao, H. Wang, X. Liu, P.R. Haydel, T. Li, J. Chen, P. Huang, Q. Xiao, T. Tatsumi, J. Wang, Single-crystalline hierarchically-porous TS-1 zeolite catalysts via a solid-phase transformation mechanism, *Microporous Mesoporous Mater.* 313 (2021), 110828, <https://doi.org/10.1016/j.micromeso.2020.110828>.
- [35] Q. Sun, N. Wang, Q. Bing, R. Si, J. Liu, R. Bai, P. Zhang, M. Jia, J. Yu, Subnanometric hybrid Pd-M(OH)<sub>2</sub>, M = Ni, Co, clusters in zeolites as highly efficient nanocatalysts for hydrogen generation, *Chem* 3 (2017) 477–493, <https://doi.org/10.1016/j.chempr.2017.07.001>.
- [36] Q. Sun, N. Wang, T. Zhang, R. Bai, A. Mayoral, P. Zhang, Q. Zhang, O. Terasaki, J. Yu, Zeolite-encaged single-atom rhodium catalysts: highly-efficient hydrogen generation and shape-selective tandem hydrogenation of nitroarenes, *Angew. Chem. Int. Ed.* 58 (2019) 18570–18576, <https://doi.org/10.1002/anie.201912367>.
- [37] N. Li, M. Wang, Q. You, C. Bi, H. Chen, B. Liu, M. Sun, Q. Hao, J. Zhang, X. Ma, Bolaform surfactant-directed synthesis of TS-1 zeolite nanosheets for catalytic epoxidation of bulky cyclic olefins, *Catal. Sci. Technol.* 10 (2020) 1323–1335, <https://doi.org/10.1039/C9CY02282A>.
- [38] M. Choi, K. Na, J. Kim, Y. Sakamoto, O. Terasaki, R. Ryoo, Stable single-unit-cell nanosheets of zeolite MFI as active and long-lived catalysts, *Nature* 461 (2009) 246–249, <https://doi.org/10.1038/nature08288>.
- [39] A. Glotov, A. Vutolkina, M. Artemova, N. Demikhova, E. Smirnova, E. Roldugina, A. Stavitskaya, E. Ivanov, S. Egazar'yants, V. Vinokurov, Micro-mesoporous MCM-41/ZSM-5 supported Pt and Pd catalysts for hydroisomerization of C-8 aromatic fraction, *Appl. Catal. A Gen.* 603 (2020), 117764, <https://doi.org/10.1016/j.apcata.2020.117764>.
- [40] S. Bosnar, V. Rac, D. Stojić, A. Travert, G. Postole, A. Auroux, S. Škapin, L. Damjanović-Vasilčić, J. Brionić, X. Du, S. Marković, V. Pavlović, V. Rakić, Overcoming phase separation in dual templating: a homogeneous hierarchical ZSM-5 zeolite with flower-like morphology, synthesis and in-depth acidity study, *Microporous Mesoporous Mater.* 329 (2022), 111534, <https://doi.org/10.1016/j.micromeso.2021.111534>.
- [41] H. Chen, Y. Wang, C. Sun, X. Wang, C. Wang, Synthesis of hierarchical ZSM-5 zeolites with CTAB-containing seed silicalite-1 and its catalytic performance in methanol to propylene, *Catal. Commun.* 112 (2018) 10–14, <https://doi.org/10.1016/j.catcom.2018.04.017>.
- [42] H.J. Li, X.D. Zhou, Y.H. Di, J.M. Zhang, Y. Zhang, Effect of Si-ATP/CTAB ratio on crystal morphology, pore structure and adsorption performance of hierarchical (H)

- ZSM-11 zeolite, Microporous Mesoporous Mater. 271 (2018) 146–155, <https://doi.org/10.1016/j.micromeso.2018.05.039>.
- [43] W. Xu, T. Zhang, R. Bai, P. Zhang, J. Yu, A one-step rapid synthesis of TS-1 zeolites with highly catalytically active mononuclear  $\text{TiO}_6$  species, J. Mater. Chem. A 8 (2020) 9677–9683, <https://doi.org/10.1039/c9ta13851j>.
- [44] Z. Chen, J. Wang, K. Shen, R. Wang, H. Liu, X. Huang, Z. Tang, Y. Yu, Y. Liu, In-depth understanding the role of seeds in the synthesis of TS-1, Appl. Catal. A Gen. 591 (2020), 117403, <https://doi.org/10.1016/j.apcata.2019.117403>.
- [45] M. Liu, Z. Chang, H. Wei, B. Li, X. Wang, Y. Wen, Low-cost synthesis of size-controlled TS-1 by using suspended seeds: from screening to scale-up, Appl. Catal. A Gen. 525 (2016) 59–67, <https://doi.org/10.1016/j.apcata.2016.07.006>.
- [46] G. Xiong, Q. Jia, Y. Cao, L. Liu, Z. Guo, The effect of acid treatment on the active sites and reaction intermediates of the low-cost TS-1 in propylene epoxidation, RSC Adv. 7 (2017) 24046–24054, <https://doi.org/10.1039/C7RA02983G>.
- [47] M. Zhu, C. Zhu, D. Wu, X. Wang, H. Wang, J. Gao, H. Huang, C. Shi, Y. Liu, Z. Kang, Efficient photocatalytic water splitting through titanium silicalite stabilized CoO nanodots, Nanoscale 11 (2019) 15984–15990, <https://doi.org/10.1039/C9NR05057D>.
- [48] X. Shao, Y. Zhang, J. Li, Z. Wang, X. Zhang, L. Wang, W. Yuan, H. Wang, Seed-sol-assisted construction of a coffin-shaped multilamellar ZSM-5 single crystal using CTAB, Chem. Commun. 57 (2021) 10624–10627, <https://doi.org/10.1039/D1CC04620A>.
- [49] M. Liu, J. Li, W. Jia, M. Qin, Y. Wang, K. Tong, H. Chen, Z. Zhu, Seed-induced synthesis of hierarchical ZSM-5 nanosheets in the presence of hexadecyl trimethyl ammonium bromide, RSC Adv. 5 (2015) 9237–9240, <https://doi.org/10.1039/C4RA14955F>.
- [50] X. Liang, X. Peng, C. Xia, H. Yuan, K. Zou, K. Huang, M. Lin, B. Zhu, Y. Luo, X. Shu, Improving Ti incorporation into the BEA framework by employing ethoxylated chlorotitanate as Ti precursor: postsynthesis, characterization, and incorporation mechanism, Ind. Eng. Chem. Res. 60 (2021) 1219–1230, <https://doi.org/10.1021/acs.iecr.0c04375>.
- [51] N. Hoeven, G. Mali, M. Mertens, P. Cool, Design of Ti-Beta zeolites with high Ti loading and tuning of their hydrophobic/hydrophilic character, Microporous Mesoporous Mater. 288 (2019), 109588, <https://doi.org/10.1016/j.micromeso.2019.109588>.
- [52] Y. Hu, K. Wang, C. Han, T. Wang, G. Luo, Liquid-liquid microdispersion method for the synthesis of TS-1 free of extra-framework Ti species, Ind. Eng. Chem. Res. 58 (2019) 12010–12017, <https://doi.org/10.1021/acs.iecr.9b01764>.
- [53] W. Dai, C. Kouvatas, W. Tai, G. Wu, N. Guan, L. Li, V. Valtchev, Platelike MFI crystals with controlled crystal faces aspect ratio, J. Am. Chem. Soc. 143 (2021) 1993–2004, <https://doi.org/10.1021/jacs.0c11784>.
- [54] I. Khan, X. Chu, Y. Liu, S. Khan, L. Bai, L. Jing, Synthesis of  $\text{Ni}^{2+}$  cation modified TS-1 molecular sieve nanosheets as effective photocatalysts for alcohol oxidation and pollutant degradation, Chin. J. Catal. 41 (2020) 1589–1602, [https://doi.org/10.1016/S1872-2067\(20\)63555-0](https://doi.org/10.1016/S1872-2067(20)63555-0).
- [55] W. Qian, S. Xu, X. Zhang, C. Li, W. Yang, C.R. Bowen, Y. Yang, Differences and similarities of photocatalysis and electrocatalysis in two-dimensional nanomaterials: strategies, traps, applications and challenges, Nano-Micro Lett. 13 (2021) 156, <https://doi.org/10.1007/s40820-021-00681-9>.
- [56] N.K. Kumawat, W. Tress, F. Gao, Mobile ions determine the luminescence yield of perovskite light-emitting diodes under pulsed operation, Nat. Commun. 12 (2021) 4899, <https://doi.org/10.1038/s41467-021-25016-5>.
- [57] X. Zhang, Z. Jin, Y. Li, S. Li, G. Lu, Photocatalytic hydrogen generation over Eosin Y-Sensitized TS-1 zeolite, Appl. Surf. Sci. 254 (2008) 4452–4456, <https://doi.org/10.1016/j.apsusc.2008.01.038>.
- [58] Y. Yamazaki, J. Přech, Y. Kuwahara, K. Mori, J. Čejka, H. Yamashita, Catalytic and photocatalytic epoxidation over microporous titanasilicates with nanosheet or layered structure, Catal. Today 376 (2021) 28–35, <https://doi.org/10.1016/j.cattod.2020.08.034>.
- [59] C.J. Heard, L. Grajciar, F. Uhlík, M. Shamzhy, M. Opanasenko, J. Čejka, P. Nachtigall, Zeolite (in)stability under aqueous or steaming conditions, Adv. Mater. 32 (2020), 2003264, <https://doi.org/10.1002/adma.202003264>.
- [60] B.T. Barrocas, J. Přech, M.F. Edelmánová, E. Szaniawska, K. Kočí, J. Čejka, Titanosilicates enhance carbon dioxide photocatalytic reduction, Appl. Mater. Today 26 (2022), 101392, <https://doi.org/10.1016/j.apmt.2022.101392>.
- [61] M. Takeuchi, S. Sakai, A. Ebrahimi, M. Matsuoka, M. Anpo, Application of highly functional Ti-oxide-based photocatalysts in clean technologies, Top. Catal. 52 (2009) 1651–1659, <https://doi.org/10.1007/s11244-009-9300-7>.
- [62] J. Zhou, J. Li, L. Kan, L. Zhang, Q. Huang, Y. Yan, Y. Chen, J. Liu, S.L. Li, Y.Q. Lan, Linking oxidative and reductive clusters to prepare crystalline porous catalysts for photocatalytic  $\text{CO}_2$  reduction with  $\text{H}_2\text{O}$ , Nat. Commun. 13 (2022) 4681, <https://doi.org/10.1038/s41467-022-32449-z>.
- [63] H. Yin, F. Su, C. Luo, L. Zhu, W. Zhong, L. Mao, K. You, D. Yin, Visible-light-mediated remote aliphatic C–H oxyfunctionalization over  $\text{CuCl}_2$  decorated hollowed-TS-1 photocatalysts, Appl. Catal. B Environ. 302 (2022), <https://doi.org/10.1016/j.apcatb.2021.120851>.